

***In Situ* Monitoring of the Thermal-Annealing Effect in a Monolayer of MoS₂**Liqin Su,¹ Yifei Yu,² Linyou Cao,² and Yong Zhang^{1,*}¹*Department of Electrical and Computer Engineering, University of North Carolina at Charlotte, Charlotte, North Carolina 28223, USA*²*Department of Materials Science and Engineering, North Carolina State University, Raleigh, North Carolina 27695, USA*

(Received 12 October 2016; published 10 March 2017)

We perform *in situ* two-cycle thermal-annealing studies for a transferred CVD-grown monolayer MoS₂ on a SiO₂/Si substrate, using spatially resolved micro-Raman and photoluminescence spectroscopy. The evolution in film morphology and film-substrate bonding is continuously monitored by Raman spectroscopy. After the thermal cycling and being annealed at 305 °C twice, the film morphology and film-substrate bonding are significantly modified, which together with the removal of polymer residues causes major changes in the strain and doping distribution over the film, and thus the optical properties. Before annealing, the strain associated with ripples in the transferred film dominates the spatial distributions of the photoluminescence peak position and intensity over the film; after annealing, the variation in film-substrate bonding, affecting both strain and doping, becomes the leading factor. This work reveals that the film-substrate bonding, and thus the strain and doping, is nonstationary under thermal stress, which is important for understanding the substrate effects on the optical and transport properties of the 2D material and their impact on device applications.

DOI: [10.1103/PhysRevApplied.7.034009](https://doi.org/10.1103/PhysRevApplied.7.034009)**I. INTRODUCTION**

Single-layer molybdenum disulfide (MoS₂), along with other two-dimensional (2D) materials, has been shown to exhibit many unique electronic and optical properties. However, their properties are very sensitive to the perturbations from either supporting substrates or surface contaminants as well as unintended film-morphology fluctuations. Among these external perturbations, the role of the substrate is “intrinsic” and, thus, ultimately important to fundamental understanding and application of the 2D material. Numerous studies on the substrate-supported transition-metal dichalcogenide films concerned the effects of different substrate types [1–5]. It was often implicitly assumed that the substrate effects depended solely on the substrate material and the film-substrate bonding was static, thus, the obtained results were representative of the specific substrate type. However, it has been shown that on the same substrate type, variations in film morphology and film-substrate bonding strength can have major impacts on the material properties [2,4]. Furthermore, the film-substrate interactions have been shown to be nonstationary under thermal [2,4] and electrical stress [6–8], and may differ significantly for the same substrate material, but prepared differently (e.g., epitaxially grown vs transferred) [4]. Changes in surface morphology and film-substrate bonding during thermal annealing have been attributed to the unusual temperature evolution in the optical properties

[2,4], whereas alternations in the interfacial states and surface contaminants under electrical stress have been suggested to be responsible for the instability of electrical characteristics [6–8]. Therefore, the answer to a question such as how the substrate will impact the carrier saturation velocity of a 2D material is unlikely to be unique [9–11]. Furthermore, it is unclear how thermal annealing or unintended thermal stress during temperature-dependent measurements will affect the material properties, and how the interplays will be of the above-mentioned intrinsic (substrate) and extrinsic perturbations responding to the annealing.

Thermal annealing is widely used for postgrowth material treatment. Typically, the annealing effect is tested after the material is brought back to room temperature (RT), and thus how the material evolves during the annealing process is rarely known. We have previously studied the substrate effects in one single low-to-high temperature cycle up to the thermal degradation point (typically >500 °C) for MoS₂ and WS₂, which has provided valuable information about the film-substrate interaction as mentioned above [2,4]. However, these efforts could not provide the material properties at RT after the thermal cycle. In this work, we perform an *in situ* two-cycle thermal-annealing study, with the upper temperature limited to ~305 °C (much below the degradation point), on both Raman and photoluminescence (PL) characteristics of a transferred monolayer MoS₂ film on a SiO₂/Si substrate. Specifically, the measurements are carried out not only at RT before and after the first cycle, and after the second

*yong.zhang@uncc.edu

cycle, but also during the annealing cycles. This effort allows us to reveal the annealing effects on the film morphology, film-substrate bonding, and surface contaminants, the consequences of annealing to strain and doping, and the manifestations on the optical properties. Additionally, using spatially resolved μ Raman and PL we are able to study the spatial inhomogeneity of these effects. The findings have major implication on the understanding of the electronic transport properties, and tuning the material properties through substrate engineering.

The influence of the substrate on the electrical and optical properties of 2D films is typically associated with the strain and doping effects [12–14]. Raman spectroscopy is often used to probe these two effects in the transition-metal dichalcogenide films, because the two primary Raman modes, the in-plane E_{2g} mode and out-of-plane A_{1g} mode, respond differently to the two effects: E_{2g} is more sensitive to the strain than A_{1g} , approximately by a factor of 4, because the former has a much larger deformation potential than the latter [15], while A_{1g} is much more sensitive to the doping than E_{2g} , approximately by a factor of 10, because of the symmetry selection rule difference in the electron-phonon coupling between the two modes [16]. The deformation potentials under biaxial strain for the phonon modes and band gap have been estimated to be $-4.5 \text{ cm}^{-1}/\%$ for E_{2g} , $-1.0 \text{ cm}^{-1}/\%$ for A_{1g} [17], and $-70 \text{ meV}/\%$ for the band gap [18], respectively. Structural defects may introduce bound states that could either provide doping in the 2D film if they are shallow, or quench the interband recombination when they are far away from the band edges [19]. It has been proposed that charge transfer between the film and the substrate can significantly modify the doping concentration, and influence the optical properties [14,20,21]. These excessive charged carriers may couple with neutral excitons to form trions: A^- (negatively charged) and A^+ (positively charged) [22]. Furthermore, the monolayer MoS_2 is often grown by CVD and then transferred to another substrate with polymer-assisted transfer processes, leaving behind residuals on the surface of MoS_2 which is challenging to be removed. The polymer residues as well as adsorbed H_2O and O_2 are known to modify the optical and electrical properties of the film, such as the quenching of photogenerated excitons and the reduction of carrier mobility [5,23–25].

Temperature-dependent Raman scattering has been used to investigate the vibrational properties of both bulk and monolayer MoS_2 , and in general both E_{2g} and A_{1g} peaks exhibit redshift with increasing temperature [2,26–28]. Besides the fundamental interest in the vibrational properties of the 2D material, we show that because of the expected nearly linear temperature dependence of the phonon frequencies for an idealistic 2D material in the elevated temperature region (above RT), the temperature-dependent Raman study can be used as an

effective probe to the film-substrate interaction [2,4,29]. For instance, in our previous work we have shown that the A_{1g} mode, and to a lesser extent also the E_{2g} mode, shows an anomalous nonlinear temperature dependence due to temperature-induced changes in the film morphology and the interaction with the substrate [2]. The similar effect occurred in graphene, which limited the study of the intrinsic temperature dependence in a lower temperature region [30].

A. Experiment

Monolayer MoS_2 is initially grown on sapphire using our previously reported CVD method with molybdenum chloride (MoCl_5) and sulfur as the precursor [31]. Briefly, the MoCl_5 powder is placed at the center of the furnace and the sulfur at the upstream entry of the furnace, while the receiving substrates are placed downstream at a distance of 1–7 cm away from the center of the furnace. The furnace is heated up to a rate of $28 \text{ }^\circ\text{C}/\text{min}$ up to $850 \text{ }^\circ\text{C}$ with Ar gas purged. High-quality and large-area MoS_2 monolayer film is synthesized on the sapphire wafer with properly controlled parameters including temperature, Ar flow rate, and the amount of precursor.

The method used to transfer as-grown on-sapphire MoS_2 to a Si wafer coated with 300-nm SiO_2 was reported in our previous work with the assistance of polystyrene (PS) [32]. A thin layer of PS was spin coated onto the as-grown sample, followed by a baking at $80\text{--}90 \text{ }^\circ\text{C}$ for 15 min to facilitate intimate adhesion of the PS layer with the MoS_2 film. With the assistance of a water droplet that penetrates all the way through the MoS_2 film, the PS- MoS_2 assembly was delaminated and transferred onto the SiO_2/Si substrate. After baking the transferred PS- MoS_2 assembly at proper temperature to remove the water residues, the PS was removed by rinsing with toluene several times. As shown in our previous studies [2,4], the as-transferred film exhibits weak bonding with the substrate. It has also been found that after the transfer process, molecules can be adsorbed on the film as well as trapped between the film and the substrate [33].

μ -Raman and PL measurements are performed with a Horiba LabRAM HR800 system using a 532-nm excitation laser with a $50\times$ -long working-distance lens ($\text{NA} = 0.5$), and the laser power used is $\leq 1 \text{ mW}$, sufficiently low not to cause significant shifting in both Raman modes. All the PL and Raman measurements are carried out in a Linkam TS1500 heating system. In the temperature-dependent Raman measurement, N_2 gas is purged through the heating chamber at a very low flow rate to avoid the oxidation of MoS_2 film [2,4,34]. The temperature is elevated gradually to $305 \text{ }^\circ\text{C}$ with a step of $20 \text{ }^\circ\text{C}$ at a rate of $10 \text{ }^\circ\text{C}/\text{min}$. At each temperature, the spectrum is acquired after allowing at least 5 min for thermal stabilization of the sample. The sample is annealed at $305 \text{ }^\circ\text{C}$ for 30 min, and cooled down to room temperature naturally with N_2 purging.

II. RESULTS AND DISCUSSION

Figure 1(a) shows the optical image of a transferred MoS₂ film on which spatially resolved Raman and PL measurements are performed in a marked area of 20 $\mu\text{m} \times 20 \mu\text{m}$. The sample contains a visible long wrinkle (in darker color near the bottom of the marked area) and many less-visible shorter ones, and a crack (in lighter color near the lower left corner of the marked area). In order to see the shorter wrinkles more apparently, an AFM image (not the same area as the marked one) is shown in Fig. 1(b), and the wrinkles are less than 12 nm in height [Fig. 1(c)]. The primary focus of this work is to understand the behavior of the general area, while the behavior of the large wrinkle will only be briefly addressed when appropriate. Raman spectroscopy is a convenient and effective method to determine the thickness of the film through the frequency difference between A_{1g} and E_{2g} modes—the difference should be $<20 \text{ cm}^{-1}$ for monolayer [35]. Figure 1(d) shows a typical Raman spectrum of the sample, and the frequencies of E_{2g} and A_{1g} are $\sim 386 \text{ cm}^{-1}$ and $\sim 404 \text{ cm}^{-1}$, respectively. The spatial mapping of the frequency difference over the marked area in Fig. 1(a) shows a maximum of 19.2 cm^{-1} [Fig. 1(e)], indicating the film overall is indeed monolayer. Figure 1(f) shows RT PL

spectra at different laser powers. At 25 μW only one peak at $\sim 1.88 \text{ eV}$ is observed; however, a new peak appears at $\sim 1.85 \text{ eV}$ as the power increases to 150 μW , and then dominates the PL spectrum as the power increases further to 1 mW. The lower-energy component cannot be assigned as the emission related to impurity or defect states. If it were the case, at the low excitation level, the electrons would tend to occupy these states prior to the conduction band, thus the lower-energy peak would be dominant; furthermore, the intensity ratio of the lower-energy peak to the higher-energy peak would decrease with increasing laser power, because of the state filling effect. On the contrary, the proportion of the lower-energy peak increases with increasing laser power. As mentioned above, the free carriers can couple with neutral excitons to form trions, and the emission of trions increases with increasing carrier density [14,36]. Therefore, the lower-energy peak at 1.85 eV can be assigned as A^- . Another weak PL peak at $\sim 2.02 \text{ eV}$ can also be seen, and is assigned as a B exciton. The A and B excitons originate from the splitting of the valence band at the K point [37].

Figure 2 presents the RT Raman and PL mapping results of integrated intensity and peak position before annealing the film. The Raman intensity data [Figs. 2(a) and 2(b)] show overall uniform distribution over the film except for

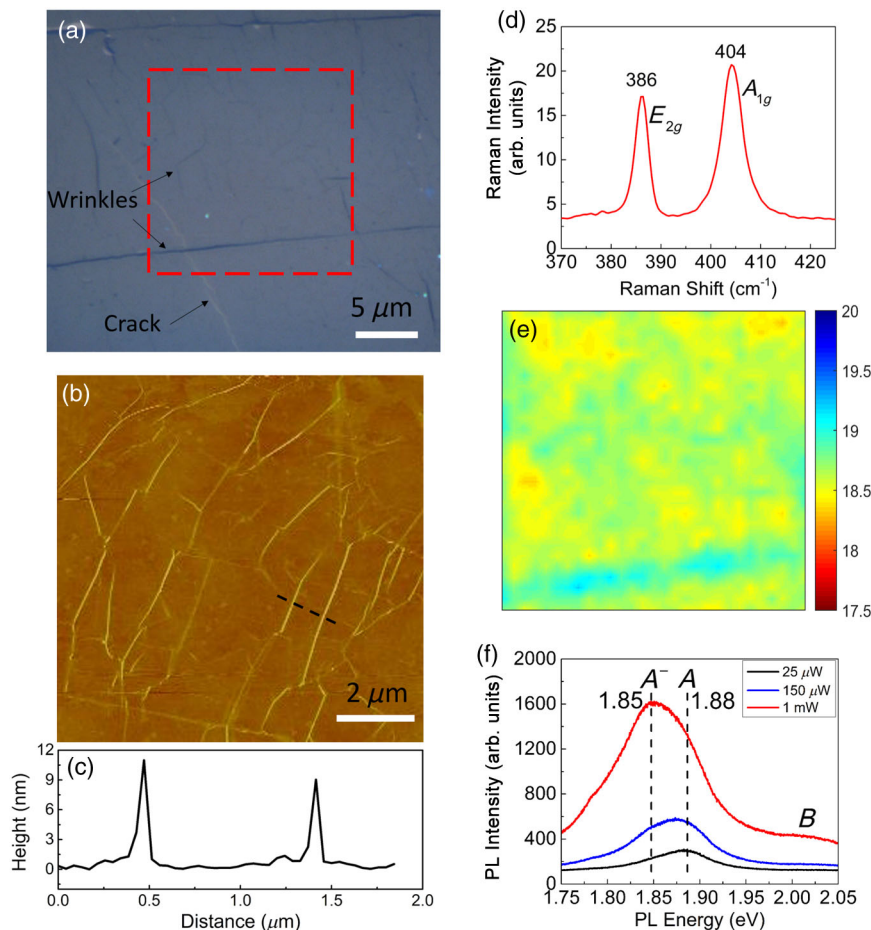


FIG. 1. Room-temperature characterization of a transferred monolayer MoS₂ film on a SiO₂/Si substrate. (a) Optical image. (b) Atomic force microscopy (AFM) image (not the same area as the marked one). (c) The height profile extracted from the AFM image along the dashed line labeled in panel (b). (d) Typical Raman spectrum. (e) The spatial mapping (20 $\mu\text{m} \times 20 \mu\text{m}$) of the frequency difference between E_{2g} and A_{1g} in the area marked in panel (a). (f) Typical power-dependent PL spectra.

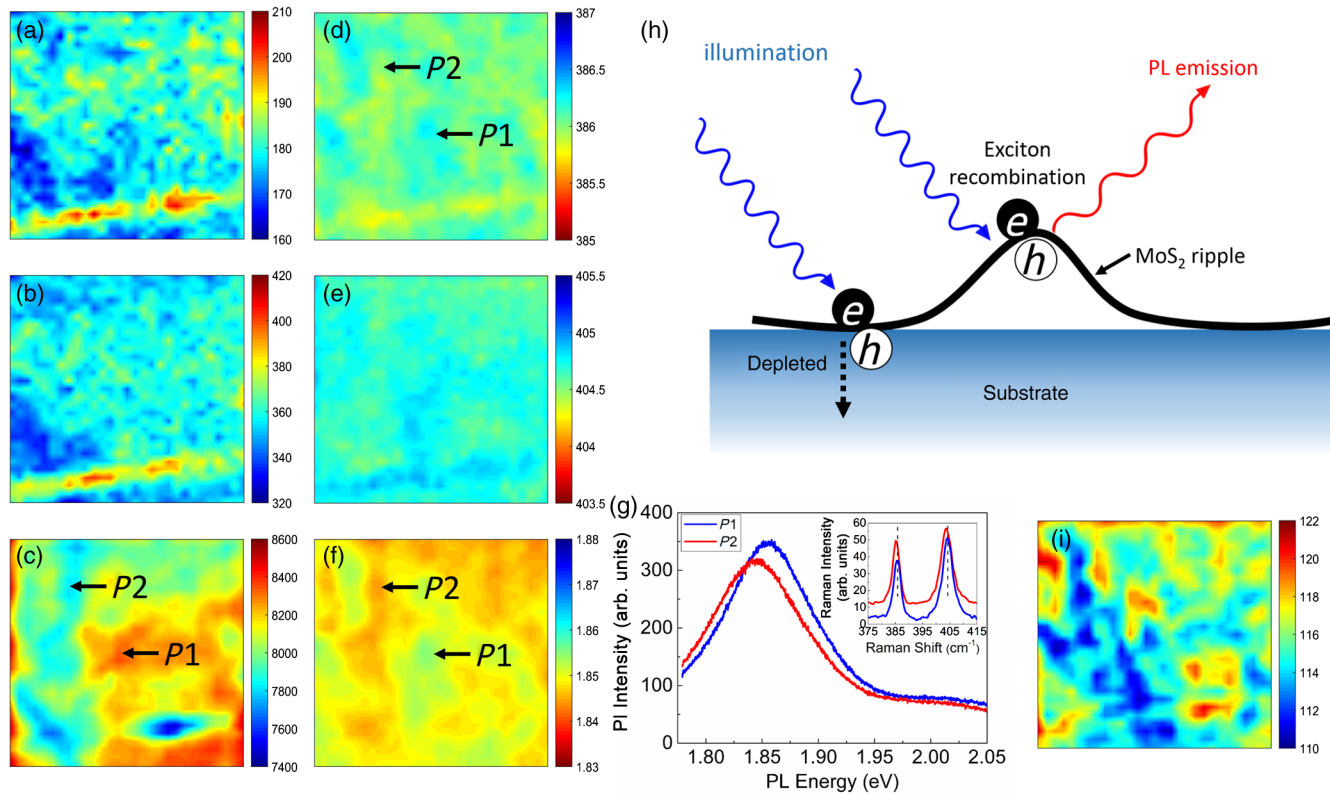


FIG. 2. Room-temperature Raman and PL mapping results before the first thermal annealing. (a)–(c) Intensity maps of (a) E_{2g} mode, (b) A_{1g} mode, and (c) PL. (d)–(f) The maps of (d) E_{2g} frequency, (e) A_{1g} frequency, and (f) PL energy. (g) PL and Raman spectra of two locations $P1$ and $P2$. (h) Schematic illustration of PL intensity inhomogeneity. (i) The FWHM map of PL. Note that (a)–(c) use a “blue-to-red” color code for the intensity maps, while (d)–(f) use a “red-to-blue” color code for frequency or energy maps.

along the wrinkles with higher intensity and near the crack with lower intensity. The wrinkled regions (appearing as lines in optical and AFM images) tend to have larger effective absorbing areas, resulting in stronger Raman intensity. The PL intensity mapping shows a more significant variation, $\sim 20\%$ [Fig. 2(c)]. The Raman and PL peak-position data are shown in Figs. 2(d)–2(f), with maximum variations of $\sim 0.6 \text{ cm}^{-1}$ for the E_{2g} mode, $\sim 0.7 \text{ cm}^{-1}$ for the A_{1g} mode, and $\sim 12 \text{ meV}$ for PL, respectively. There appears a general correlation, revealed by the similar patterns, between E_{2g} Raman frequency and PL energy over the mapped area, i.e., the area with lower (higher) Raman frequency [Fig. 2(d)] shows lower (higher) PL energy [Fig. 2(f)]. Interestingly, the wrinkles shown in the marked area [Fig. 1(a)] generally match the areas with lower E_{2g} frequency and PL energy. Therefore, the origin of the nonuniform E_{2g} frequency and PL energy is most likely due to the morphology fluctuations over the MoS₂ monolayer, i.e., the transferred film is not laid down perfectly flat but with many microscopic scale ripples and elongated wrinkles, where wrinkles can be considered as ripples with more abrupt changes in morphology. Thus, if the strain is responsible for the variations, using the deformation potentials given above, the corresponding maximum strain

differences derived from the data of Figs. 2(d)–2(f), would be 0.13%, 0.7%, and 0.17%, respectively, for E_{2g} , A_{1g} , and PL, respectively. Apparently, the estimated strain difference from A_{1g} is much larger in magnitude than those from E_{2g} and PL, suggesting that the doping effect, which preferentially affects A_{1g} , could play a significant role in the monolayer MoS₂ film. Notably, for A_{1g} along the large wrinkle, it is blueshifted with respect to the general area, in contrast to the redshift for E_{2g} . Usually, the inhomogeneity of strain distribution can cause exciton localization as observed in both bulk and 2D materials, where PL is enhanced at lower band-gap areas [12,18,38]. Such anticorrelation between the emission intensity and energy occurs under the conditions that the excitons are sufficiently mobile and nonradiative recombination rates are comparable between the high and low energy regions. On the contrary, the PL mapping data show generally positive correlation between the intensity [Fig. 2(c)] and the peak energy [Fig. 2(f)]. For instance, the region $P1$ ($P2$) marked in Figs. 2(c), 2(d), and 2(f) exhibits higher (lower) PL intensity and energy as well as E_{2g} Raman frequency, as shown in Fig. 2(g). As pointed out above, the higher PL energy and Raman frequency is mainly attributed to the presence of more compressive strain or less tensile strain.

The strain variation could be caused by the nonplanar film morphology, which likely occurred in the film transfer process, in the forms of wrinkles and ripples as shown schematically in Fig. 2(h). The charge transfer between the film and substrate has been found to be sensitive to the details of the film-substrate contact [1]. At the interface of SiO₂ and MoS₂, interfacial states are formed due to the presence of high-density dangling bonds on the surface of SiO₂. Electrons tend to be trapped in these states [39,40]. In the nonrippled regions, the photogenerated nonequilibrium carriers will more likely be depleted through the film-substrate interface. In the rippled regions, where the PL energy is higher, in principle, the photogenerated carriers can drift to the regions with lower energies. However, because of the limited carrier mobility of the film and/or high carrier depletion rate in the lower-energy regions, the PL intensity in the rippled regions turns out to be higher. Note that the PL peak position in the mapping [Fig. 2(f)] is associated with A⁻ trion rather than A exciton, because maximum PL peak position over the mapped area is 1.855 eV, implying that the A⁻ emission dominates the PL emission. Figure 2(i) shows the map of PL full width at half maximum (FWHM) over the mapped area. The FWHM of the A⁻ peak is found unaffected by the substrate [21], and we also find a small variation of 115 ± 5 meV over the mapped area. These results indicate that the MoS₂ film has been *n*-type doped, and the origin of the doping could be the polymer residues left behind the transfer process [14,21].

Next, single-point Raman measurements are carried out on one fixed location in the film (near the center of the mapped area) over a temperature range from RT to 305 °C with a step of 20 °C. Figure 3(a) shows temperature-dependent Raman spectra, showing redshift of both *E*_{2g} and *A*_{1g} modes with increasing temperature. The change in peak position of the *E*_{2g} and *A*_{1g} modes with increasing

temperature is plotted in Figs. 3(b) and 3(c), respectively. The *E*_{2g} mode shows a very linear temperature dependence, which can be fitted well by a linear dependence:

$$\omega = \omega_0 + \chi \Delta T, \quad (1)$$

where ω_0 is the mode frequency at RT, ΔT is the temperature change relative to RT, and χ is the first-order temperature coefficient.

However, the temperature dependence of the *A*_{1g} mode is rather nonlinear and can only be described by a third-order polynomial function used in our previous paper [2]:

$$\omega(T) = \omega_0 + \chi_1 \Delta T + \chi_2 (\Delta T)^2 + \chi_3 (\Delta T)^3, \quad (2)$$

where χ_1 , χ_2 , and χ_3 are the first-, second-, and third-order temperature coefficients. The temperature coefficients of the *E*_{2g} and *A*_{1g} modes obtained from the first temperature cycle are listed in Table I, compared with the previously obtained bulk values. The results are in a good agreement with our previous work [2]. As discussed there, the nonlinear temperature dependence of the *A*_{1g} mode is attributed to the change in film morphology, while the *E*_{2g} mode is not sensitive to morphology. With increasing temperature, the film tends to change its morphology due to the mismatch in thermal expansion coefficients (TECs) between the SiO₂ substrate and the MoS₂ monolayer. At RT, SiO₂ TEC is $\sim 0.5 \times 10^{-6} \text{ K}^{-1}$, much smaller than that of monolayer MoS₂ $\sim 7 \times 10^{-6} \text{ K}^{-1}$, and increases with increasing temperature at a much smaller rate than MoS₂ [41,42]. Therefore, the strain in the MoS₂ film tends to accumulate with increasing temperature, and eventually goes beyond the confinement force of van der Waals bonding between the film and substrate, resulting in the change of the film morphology. A similar result has also been observed in graphene and WS₂ [4,30]. The film morphology change with increasing temperature leads to the change in the mechanical coupling of the MoS₂ film with a SiO₂ substrate [2,4]. With increasing temperature, the contact between the MoS₂ film and the substrate becomes more uniform and closer, leading to a greater extent of charge transfer between the film and the substrate or through interfacial states. The accelerated *A*_{1g} redshift with increasing temperature suggests increasing the equilibrium electron density, which could be due to enhanced charge injection from the substrate into the film and decomposition of adsorbed contaminants. Therefore, the first-cycle annealing process actually modifies the film morphology and gets rid of at least most polymer residues, on the surface and/or between the film and the substrate, from the transfer process as well as adsorbed H₂O and O₂.

After reaching 305 °C, the sample is annealed for 30 min and then cooled down to RT. The Raman and PL mappings are carried out again with the results shown in Fig. 4. Except for along the long wrinkle, the intensity maps of

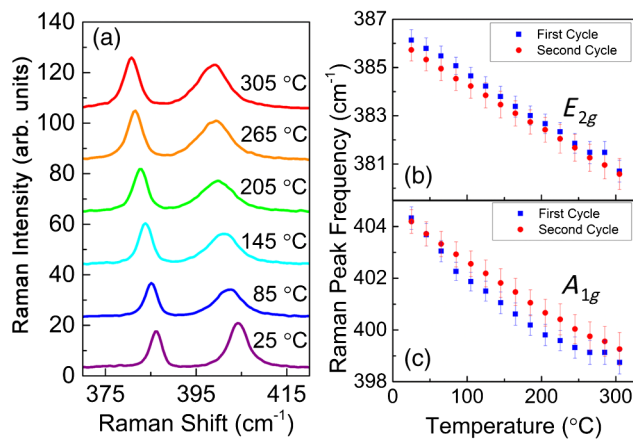


FIG. 3. Raman data taken during two thermal-annealing cycles. (a) Representative Raman spectra at selected temperatures in the first cycle. (b), (c) Temperature dependence of (b) *E*_{2g} and (c) *A*_{1g} frequency for both cycles.

TABLE I. Temperature coefficients of E_{2g} and A_{1g} modes for both cycles.

	E_{2g}		A_{1g}	
	χ	χ_1	χ_2	χ_3
First cycle	-0.0192 $\pm 3.2 \times 10^{-4}$	-0.0390 $\pm 3.5 \times 10^{-3}$	6.97×10^{-5} $\pm 2.4 \times 10^{-5}$	-3.69×10^{-8} $\pm 4.8 \times 10^{-8}$
Second cycle	-0.0183 $\pm 8.6 \times 10^{-5}$	-0.0198 $\pm 1.4 \times 10^{-3}$	-5.74×10^{-6} $\pm 9.8 \times 10^{-6}$	4.18×10^{-8} $\pm 2.0 \times 10^{-8}$
Bulk (Ref. [2])	-0.0221 $\pm 8.9 \times 10^{-4}$	-0.0197 $\pm 8.9 \times 10^{-4}$		

both E_{2g} and A_{1g} modes [Figs. 4(a) and 4(b)] become more uniform compared with those before the annealing [Figs. 2(a) and 2(b)], while the overall PL intensity [Fig. 4(c)] increases. As mentioned above, the annealing process can not only change the film morphology and strain, but it can also burn off the polymer residues, accounting for the overall redshift of E_{2g} [Fig. 4(d)] and the blueshift of PL energy [Fig. 4(f)] after the annealing. The TEC mismatch between the film and the SiO_2 substrate will introduce tensile strain after cooling down to RT, leading to the redshift of E_{2g} , although less significant for A_{1g} . However, the overall redshift is actually more significant for A_{1g} , which should be explained as being caused by the doping effect of broken-down polymer residues. As for PL, the removal of polymer residues and other contaminants on the film eliminates the nonradiative

recombination channels to the excited carriers, leading to not only the blueshift of PL energy but also the increase of PL intensity. The pattern of the PL intensity map now becomes very different from that before the annealing [Fig. 2(c)] and does not correspond to the pattern of the E_{2g} frequency map [Fig. 4(d)] anymore, indicating that the doping effect has gradually turned into the dominant factor of the PL behavior. In fact, improved overall uniformity in the Raman frequency maps for both E_{2g} and A_{1g} seems to suggest that the small ripples that initially contributed to the PL intensity inhomogeneity have been mostly removed after the annealing.

We then perform the second-cycle temperature-dependent Raman measurements at the same location as in the first cycle. The Raman frequency shifts of E_{2g} and A_{1g} modes are also plotted in Figs. 3(b) and 3(c) to make

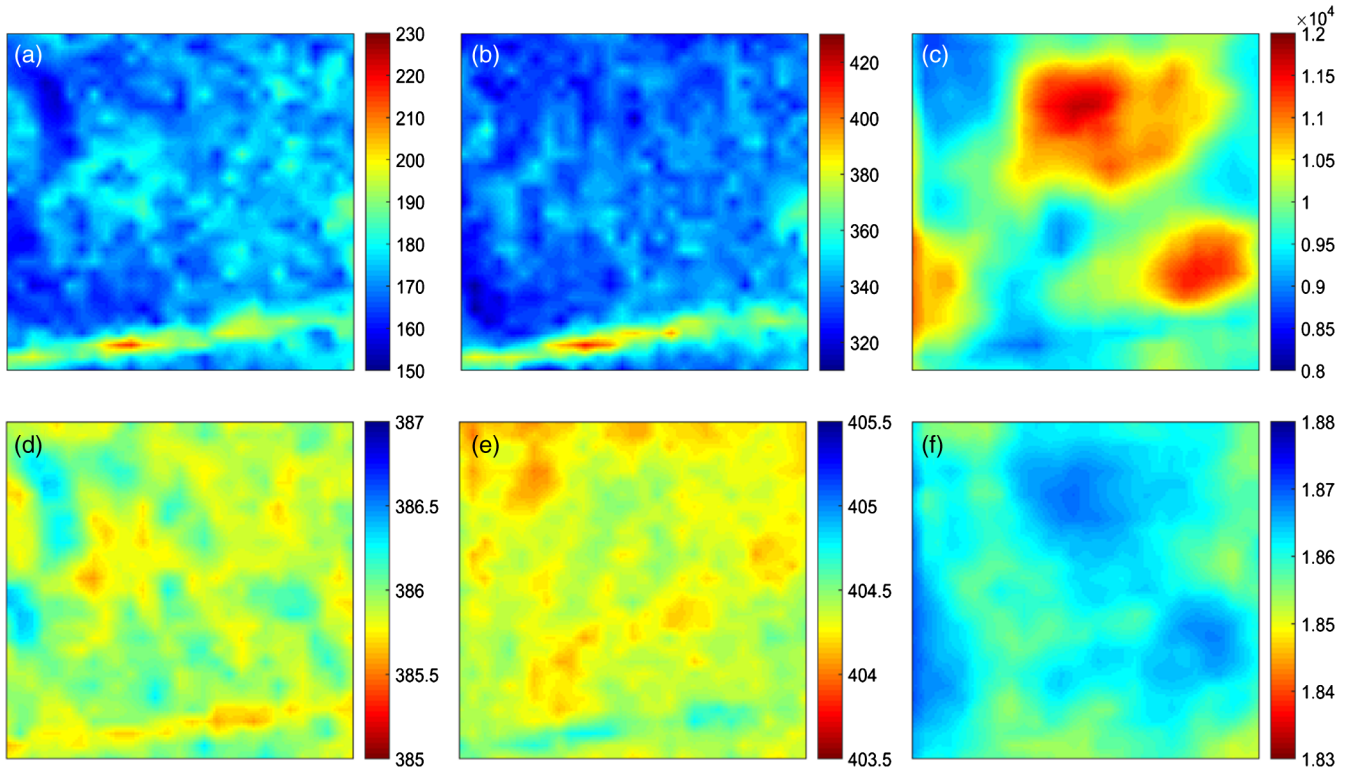


FIG. 4. Room-temperature Raman and PL mapping results after the first thermal annealing. (a)–(c) Intensity maps of (a) E_{2g} mode, (b) A_{1g} mode, and (c) PL. (d)–(f) The maps of (d) E_{2g} frequency, (e) A_{1g} frequency, and (f) PL energy.

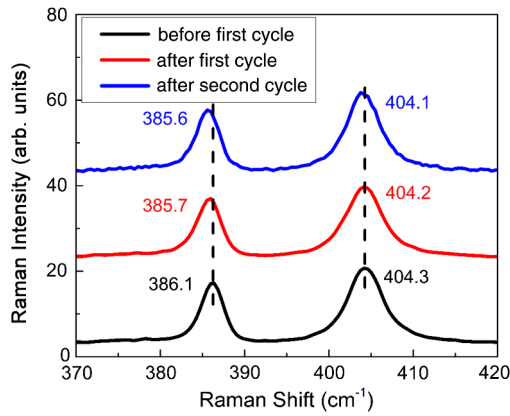


FIG. 5. Comparison of Raman spectra taken before and after the first cycle and after the second cycle on the same location. The spectra are shifted vertically for clarity.

direct comparison with the first cycle. Similar to the results of the first cycle, the E_{2g} mode shows a nearly linear temperature dependence, although with a slightly smaller slope than in the first cycle, which can be explained by the small tensile strain created by the first cycle. Whereas, the A_{1g} still remains nonlinear but to a much lesser extent than that in the first cycle due to morphology change and reduced doping level in the film. Its first-order temperature coefficient is almost halved compared to the first-cycle result, becoming very close to the bulk value, as a result of morphology change and reduced doping level in the film. The fitting results are listed in Table I. After the first-cycle annealing, the morphology of the film has been modified, i.e., the contact with the substrate has been improved, resulting in the changes in not only the doping

concentration but also the strain distribution in the film. It is worth noting that annealing at 305 °C does not introduce damage or decomposition to the MoS₂ monolayer, because the Raman intensity after two thermal cycles does not show significant change, as shown in Fig. 5.

At the end of the second round, the film is annealed at 305 °C for one hour to further remove the possible remaining polymer residues, then returned to RT. Raman and PL mappings are performed again at RT, and the results are shown in Fig. 6 with mapping data of Raman and PL: peak positions [Figs. 6(a)–6(c)] and PL intensity [Fig. 6(d)]. The maximum spatial variations of Raman and PL peak positions are found to be $\sim 1 \text{ cm}^{-1}$ for E_{2g} , $\sim 0.7 \text{ cm}^{-1}$ for A_{1g} , and $\sim 15 \text{ meV}$ for PL, respectively, over the MoS₂ film. The E_{2g} variation can be explained by the strain, yielding a range of $\sim 0.22\%$, which is larger than that before the first cycle where it is due to the morphology fluctuation in the film and also that after the first cycle the bonding with the substrate has been created. By comparing to the mapping data before and after the second cycle, the E_{2g} frequency map [Fig. 4(d) vs Fig. 6(a)] on average exhibits a redshift in Raman frequency, with the top part of the mapped area showing more shift than the lower part. The difference could reflect the variation of film-substrate bonding strength. For the top part, the bonding is stronger so that annealing generates more tensile strain in the film when cooled down to RT. The A_{1g} frequency map [Fig. 6(b)] shows an overall blueshift compared to that before the second cycle [Fig. 4(e)], and becomes somewhat similar to that before the first annealing [Fig. 2(e)], which could be explained by the charge exchange with the substrate and indicate that the charge exchange is rather

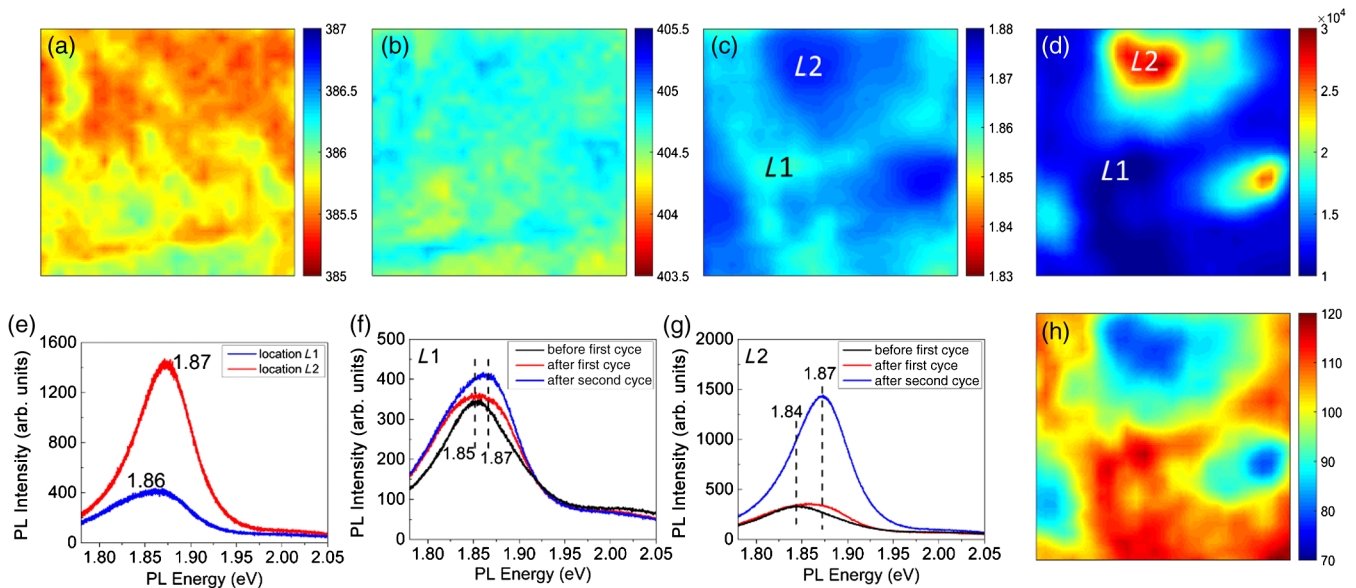


FIG. 6. Room-temperature Raman and PL mapping results after the second annealing cycle. (a)–(c) The maps of (a) E_{2g} frequency, (b) A_{1g} frequency, and (c) PL energy. (d) The map of PL intensity. (e) PL spectra of two locations L1 and L2. (f),(g) The PL spectrum comparison with those before the first annealing cycle at (f) L1 and (g) L2. (h) The FWHM map of PL spectra.

sensitive to the film-substrate bonding. For the PL mapping, compared with the results after the first annealing cycle, the PL energy is overall further blueshifted and the PL quantum yield is also further increased. After the second thermal-annealing cycle, the remaining polymer residues on the surface are further removed, which in turn reduces the nonradiative recombination in the film, giving rise to overall higher PL quantum yields than those before the

second cycle. Although improved contact with the substrate might enhance the carrier depletion through the substrate, the contaminant removal seems to be dominant in affecting the overall PL intensity. Figure 6(e) compares the PL spectra from two locations: $L1$ (a general point) and $L2$ (a special point), as marked in Figs. 6(c) and 6(d). The PL intensity at $L2$ is higher than that at $L1$, so is the PL energy at $L2$ higher than at $L1$. In fact, after the first cycle, the

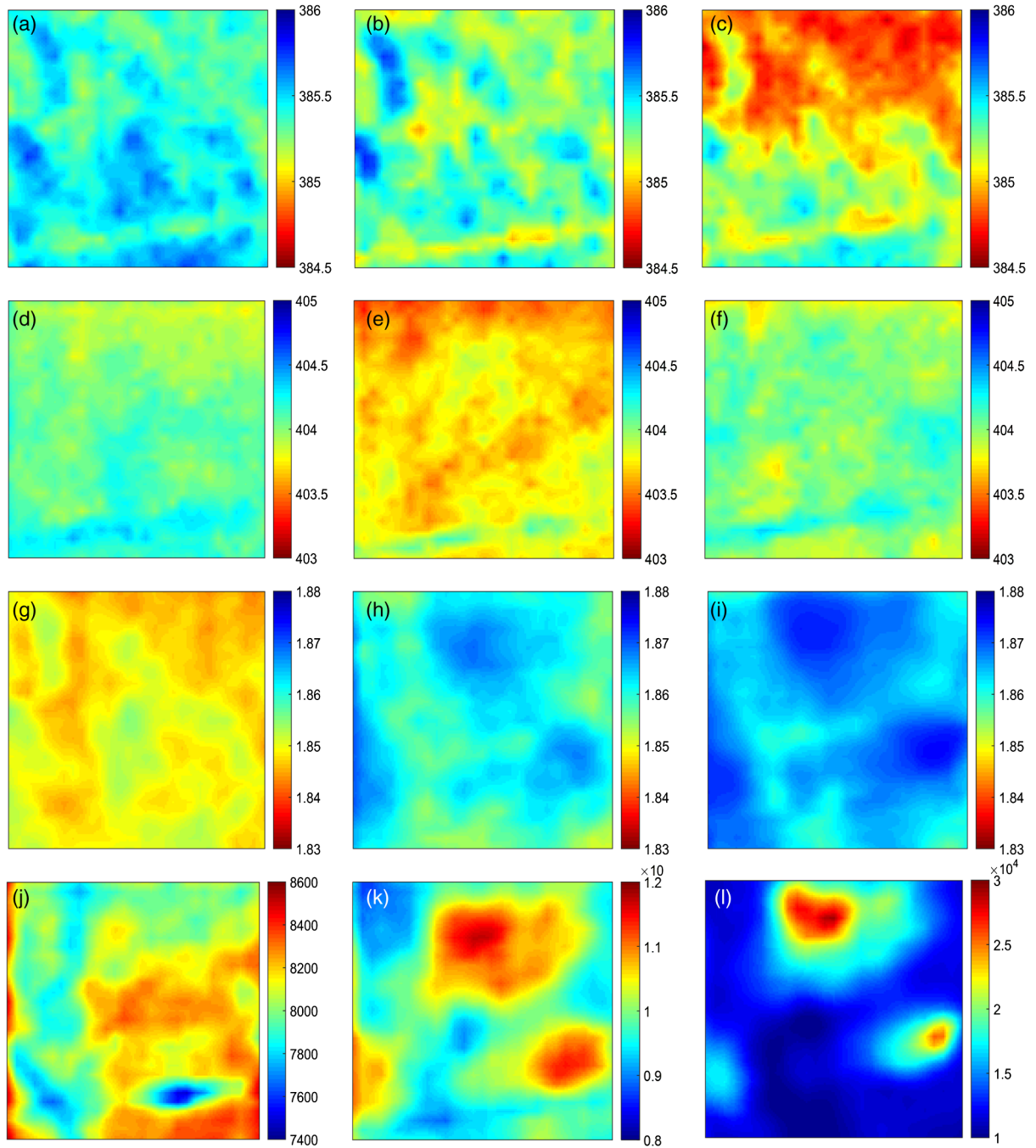


FIG. 7. Side-by-side comparisons of Raman and PL mapping data before the first cycle (left column), before the second cycle (middle column), and after the second cycle (right column). (a)–(c) Maps of E_{2g} Raman frequency. (d)–(f) Maps of A_{1g} Raman frequency. (g)–(i) Maps of PL peak energy. (j)–(l) Maps of integrated PL intensity.

general area around $L2$ already shows stronger PL, although spatially less concentrated [Fig. 4(c)]. After the first cycle, the film morphology is already modified, which significantly affects the charge doping level of the film. After the second annealing, the film morphology further evolves, and the size of the high-intensity region is reduced. We suggest that $L2$ is a buckled region with least contact with the substrate, whereas $L1$ is a general point with stronger bonding with the substrate. The peak energy of $L2$ is 1.87 eV, close to the A excitonic emission, indicating that the removal of polymer residues reduces the trion concentration in the film, hence an increase in the A excitonic recombination rate. Whereas, at $L1$, though the polymer residues have been removed after annealing, the closer contact of the film with the substrate would deplete the electrons through the interfacial states, resulting in much lower PL intensity as well as the emission energy than those at $L2$. Figures 6(f) and 6(g) compare the PL spectra of the two locations before and after the first annealing cycle and after the second annealing cycle. The comparison clearly shows that the PL peak energy gradually shifts from the A^- transition to A after two thermal-annealing cycles, and the PL intensity at $L1$ after the second cycle does not show as significant an increase as that at $L2$, which almost quadruples the intensity. Additionally, the increase of PL intensity attributed to the A excitonic recombination could imply the improvement of the conductivity of the MoS_2 film after annealing, because the free carriers interact with impurities to a lesser extent, i.e., increasing the lifetime of free carriers. Figure 6(h) shows the FWHM map of PL after the second cycle, and the regions with higher (lower) PL peak energies exhibit smaller (larger) FWHMs. Compared to the FWHM map before the first cycle [Fig. 2(i)], the FWHM at $L2$ decreases to 80 meV while that at $L1$ remains similar, which from another point of view supports the variation of doping concentration over the film.

We emphasize that the 2D film and the substrate should be treated as a complex system. Multiple competitive effects, including the film-substrate bonding, film morphology, and chemical residuals, affect the film properties. The interplay of these effects depends on not only the substrate type but also the preparation method.

For the transferred film studied in this work, thermal annealing has multiple effects. (1) Changing the film morphology: This effect on one hand has a direct consequence in changing the film properties, and on the other hand modifies the film-substrate contact or bonding, which in turn may change the film properties. (2) Changing film-substrate bonding: This is a more subtle effect to recognize. Even for the ideal case where a film is transferred to a flat surface with no buckling, the bonding with the substrate will still be modified (typically enhanced) with increasing temperature. After returning to room temperature, the state of the film is then changed. The situation is qualitatively similar to the formation of strain in an epitaxially grown

film that is grown at a higher temperature and then cooled down to room temperature [4]. (3) Removing of chemical residuals associated with the transfer: Effects (1) and (2) will change the strain and doping in the film, and effect (3) will primarily change the doping condition. Annealing-induced tensile strain leads to the E_{2g} frequency being redshifted. Reduction in the doping level leads to the PL energy being blueshifted (dominating over the strain effect). Removal of chemical residuals enhances PL overall, but the region with closer contact with the substrate shows lower intensity. An alternative way of showing the overall annealing effects is given as Fig. 7 where Raman frequencies for E_{2g} and A_{1g} , PL energy, and intensity of the three mapping results, respectively shown in Figs. 2, 4, and 6, are displayed together side-by-side for a more direct comparison.

III. CONCLUSION

In summary, we have carried out *in situ* Raman probes in two thermal cycles as well as Raman and PL mapping before and after two-cycle annealing on a monolayer MoS_2 film transferred on a SiO_2/Si substrate to study the strain and doping effects on the electronic and optical properties of the monolayer MoS_2 . Before annealing, the film-substrate bonding is weak and highly nonuniform along with the presence of chemical contaminants, where the inhomogeneous strain in the transferred film is the major cause of the fluctuations in Raman and PL peak position, and the maximum strain difference over the film is estimated to be $\sim 0.13\%$ by the phonon shift of the E_{2g} mode. However, after annealing, the film-substrate bonding is significantly improved and the polymer residues are burned off, and the film-substrate bonding becomes the leading factor of the variations in Raman and PL peak position and intensity. The strain inhomogeneity associated with the film-substrate bonding increases to $\sim 0.22\%$. These findings suggest that the annealing process can not only modify the film morphology and the film-substrate bonding, but also remove the polymer residues from the transfer process, and hence the optical and electronic performances of the MoS_2 films can be improved or altered.

ACKNOWLEDGMENTS

Y.Z. acknowledges the support of the Bissell Distinguished Professorship. L.C. acknowledges the support of a Young Investigator Award from the Army Research Office (No. W911NF-13-1-0201).

-
- [1] D. Sercombe, S. Schwarz, O. D. Pozo-Zamudio, F. Liu, B. J. Robinson, E. A. Chekhovich, I. I. Tartakovskii, O. Kolosov, and A. I. Tartakovskii, Optical investigation of the natural electron doping in thin MoS_2 films deposited on dielectric substrates, *Sci. Rep.* **3**, 3489 (2013).

- [2] L. Su, Y. Zhang, Y. Yu, and L. Cao, Dependence of coupling of quasi 2-D MoS₂ with substrates on substrate types, probed by temperature dependent Raman scattering, *Nanoscale* **6**, 4920 (2014).
- [3] M. Buscema, G. A. Steele, H. S. J. van der Zant, and A. Castellanos-Gomez, The effect of the substrate on the Raman and photoluminescence emission of single-layer MoS₂, *Nano Res.* **7**, 561 (2014).
- [4] L. Su, Y. Yu, L. Cao, and Y. Zhang, Effects of substrate type and material-substrate bonding on high-temperature behavior of monolayer WS₂, *Nano Res.* **8**, 2686 (2015).
- [5] Y. Yu, Y. Yu, C. Xu, Y.-Q. Cai, L. Su, Y. Zhang, Y.-W. Zhang, K. Gundogdu, and L. Cao, Engineering substrate interactions for high luminescence efficiency of transition-metal dichalcogenide monolayers, *Adv. Funct. Mater.* **26**, 4733 (2016).
- [6] D. J. Late, B. Liu, H. S. S. R. Matte, V. P. Dravid, and C. N. R. Rao, Hysteresis in single-layer MoS₂ field effect transistors, *ACS Nano* **6**, 5635 (2012).
- [7] K. Cho, W. Park, J. Park, H. Jeong, J. Jang, T.-Y. Kim, W.-K. Hong, S. Hong, and T. Lee, Electric stress-induced threshold voltage instability of multilayer MoS₂ field effect transistors, *ACS Nano* **7**, 7751 (2013).
- [8] P. B. Shah, M. Amani, M. L. Chin, T. P. O'Regan, F. J. Crowne, and M. Dubey, Analysis of temperature dependent hysteresis in MoS₂ field effect transistors for high frequency applications, *Solid-State Electron.* **91**, 87 (2014).
- [9] H. Schmidt, S. Wang, L. Chu, M. Toh, R. Kumar, W. Zhao, A. H. Castro Neto, J. Martin, S. Adam, B. Özyilmaz, and G. Eda, Transport properties of monolayer MoS₂ grown by chemical vapor deposition, *Nano Lett.* **14**, 1909 (2014).
- [10] G. He, K. Ghosh, U. Singiseti, H. Ramamoorthy, R. Somphonsane, G. Bohra, M. Matsunaga, A. Higuchi, N. Aoki, S. Najmaei, Y. Gong, X. Zhang, R. Vajtai, P. M. Ajayan, and J. P. Bird, Conduction mechanisms in CVD-grown monolayer MoS₂ transistors: From variable-range hopping to velocity saturation, *Nano Lett.* **15**, 5052 (2015).
- [11] H. Ramamoorthy, R. Somphonsane, J. Radice, G. He, C. P. Kwan, and J. P. Bird, "Freeing" Graphene from its substrate: Observing intrinsic velocity saturation with rapid electrical pulsing, *Nano Lett.* **16**, 399 (2016).
- [12] A. Castellanos-Gomez, R. Roldán, E. Cappelluti, M. Buscema, F. Guinea, H. S. J. van der Zant, and G. A. Steele, Local strain engineering in atomically thin MoS₂, *Nano Lett.* **13**, 5361 (2013).
- [13] H. J. Conley, B. Wang, J. I. Ziegler, R. F. Haglund, S. T. Pantelides, and K. I. Bolotin, Bandgap engineering of strained monolayer and bilayer MoS₂, *Nano Lett.* **13**, 3626 (2013).
- [14] K. F. Mak, K. He, C. Lee, G. H. Lee, J. Hone, T. F. Heinz, and J. Shan, Tightly bound trions in monolayer MoS₂, *Nat. Mater.* **12**, 207 (2013).
- [15] C. Rice, R. J. Young, R. Zan, U. Bangert, D. Wolverson, T. Georgiou, R. Jalil, and K. S. Novoselov, Raman-scattering measurements and first-principles calculations of strain-induced phonon shifts in monolayer MoS₂, *Phys. Rev. B* **87**, 081307 (2013).
- [16] B. Chakraborty, A. Bera, D. V. S. Muthu, S. Bhowmick, U. V. Waghmare, and A. K. Sood, Symmetry-dependent phonon renormalization in monolayer MoS₂ transistor, *Phys. Rev. B* **85**, 161403 (2012).
- [17] H. Li, A. W. Contryman, X. Qian, S. M. Ardakani, Y. Gong, X. Wang, J. M. Weisse, C. H. Lee, J. Zhao, P. M. Ajayan, J. Li, H. C. Manoharan, and X. Zheng, Optoelectronic crystal of artificial atoms in strain-textured molybdenum disulphide, *Nat. Commun.* **6**, 7381 (2015).
- [18] J. Feng, X. Qian, C.-W. Huang, and J. Li, Strain-engineered artificial atom as a broad-spectrum solar energy funnel, *Nat. Photonics* **6**, 866 (2012).
- [19] W. Zhou, X. Zou, S. Najmaei, Z. Liu, Y. Shi, J. Kong, J. Lou, P. M. Ajayan, B. I. Yakobson, and J.-C. Idrobo, Intrinsic structural defects in monolayer molybdenum disulfide, *Nano Lett.* **13**, 2615 (2013).
- [20] K. Dolui, I. Rungger, and S. Sanvito, Origin of the *n*-type and *p*-type conductivity of MoS₂ monolayers on a SiO₂ substrate, *Phys. Rev. B* **87**, 165402 (2013).
- [21] N. Scheuschner, O. Ochedowski, A.-M. Kaulitz, R. Gillen, M. Schleberger, and J. Maultzsch, Photoluminescence of freestanding single- and few-layer MoS₂, *Phys. Rev. B* **89**, 125406 (2014).
- [22] J. S. Ross, S. Wu, H. Yu, N. J. Ghimire, A. M. Jones, G. Aivazian, J. Yan, D. G. Mandrus, D. Xiao, W. Yao, and X. Xu, Electrical control of neutral and charged excitons in a monolayer semiconductor, *Nat. Commun.* **4**, 1474 (2013).
- [23] H. Li, J. Wu, X. Huang, Z. Yin, J. Liu, and H. Zhang, A universal, rapid method for clean transfer of nanostructures onto various substrates, *ACS Nano* **8**, 6563 (2014).
- [24] Y.-C. Lin, C.-C. Lu, C.-H. Yeh, C. Jin, K. Suenaga, and P.-W. Chiu, Graphene annealing: How clean can it be?, *Nano Lett.* **12**, 414 (2012).
- [25] S. Tongay, J. Zhou, C. Ataca, J. Liu, J. S. Kang, T. S. Matthews, L. You, J. Li, J. C. Grossman, and J. Wu, Broad-range modulation of light emission in two-dimensional semiconductors by molecular physisorption gating, *Nano Lett.* **13**, 2831 (2013).
- [26] T. Livneh and E. Sterer, Resonant Raman scattering at exciton states tuned by pressure and temperature in 2H-MoS₂, *Phys. Rev. B* **81**, 195209 (2010).
- [27] N. A. Lanzillo, A. Glen Birdwell, M. Amani, F. J. Crowne, P. B. Shah, S. Najmaei, Z. Liu, P. M. Ajayan, J. Lou, M. Dubey, S. K. Nayak, and T. P. O'Regan, Temperature-dependent phonon shifts in monolayer MoS, *Appl. Phys. Lett.* **103**, 093102 (2013).
- [28] S. Sahoo, A. P. S. Gaur, M. Ahmadi, M. J. F. Guinel, and R. S. Katiyar, Temperature-dependent Raman studies and thermal conductivity of few-layer MoS₂, *J. Phys. Chem. C* **117**, 9042 (2013).
- [29] L. Su and Y. Zhang, Temperature coefficients of phonon frequencies and thermal conductivity in thin black phosphorus layers, *Appl. Phys. Lett.* **107**, 071905 (2015).
- [30] D. Yoon, Y.-W. Son, and H. Cheong, Negative thermal expansion coefficient of graphene measured by Raman spectroscopy, *Nano Lett.* **11**, 3227 (2011).
- [31] Y. Yu, C. Li, Y. Liu, L. Su, Y. Zhang, and L. Cao, Controlled scalable synthesis of uniform, high-quality monolayer and few-layer MoS₂ films, *Sci. Rep.* **3**, 1866 (2013).
- [32] A. Gurarlan, Y. Yu, L. Su, Y. Yu, F. Suarez, S. Yao, Y. Zhu, M. Ozturk, Y. Zhang, and L. Cao, Surface-energy-assisted

- perfect transfer of centimeter-scale monolayer and few-layer MoS₂ films onto arbitrary substrates, *ACS Nano* **8**, 11522 (2014).
- [33] Y. Huang, E. Sutter, N.N. Shi, J. Zheng, T. Yang, D. Englund, H.-J. Gao, and P. Sutter, Reliable exfoliation of large-area high-quality flakes of graphene and other two-dimensional materials, *ACS Nano* **9**, 10612 (2015).
- [34] J. Wu, H. Li, Z. Yin, H. Li, J. Liu, X. Cao, Q. Zhang, and H. Zhang, Layer thinning and etching of mechanically exfoliated MoS₂ nanosheets by thermal annealing in air, *Small* **9**, 3314 (2013).
- [35] H. Li, Q. Zhang, C. C. R. Yap, B. K. Tay, T. H. T. Edwin, A. Olivier, and D. Baillargeat, From bulk to monolayer MoS₂: Evolution of Raman scattering, *Adv. Funct. Mater.* **22**, 1385 (2012).
- [36] H. Taghinejad, M. Taghinejad, A. Tarasov, M.-Y. Tsai, A. H. Hosseinnia, P. M. Campbell, A. A. Eftekhar, E. M. Vogel, and A. Adibi, Nonlinear Raman Shift Induced by Exciton-to-Trion Transformation in Suspended Trilayer MoS₂, [arXiv:1502.00593](https://arxiv.org/abs/1502.00593).
- [37] A. Splendiani, L. Sun, Y. Zhang, T. Li, J. Kim, C.-Y. Chim, G. Galli, and F. Wang, Emerging photoluminescence in monolayer MoS₂, *Nano Lett.* **10**, 1271 (2010).
- [38] Y. Zhang, M.D. Sturge, K. Kash, B.P. van der Gaag, A. S. Gozdz, L. T. Florez, and J.P. Harbison, Temperature dependence of luminescence efficiency, exciton transfer, and exciton localization in GaAs/Al_xGa_{1-x}As quantum wires and quantum dots, *Phys. Rev. B* **51**, 13303 (1995).
- [39] W. Shockley, On the surface states associated with a periodic potential, *Phys. Rev.* **56**, 317 (1939).
- [40] W. Shockley and G. L. Pearson, Modulation of conductance of thin films of semi-conductors by surface charges, *Phys. Rev.* **74**, 232 (1948).
- [41] H. Tada, A. E. Kumpel, R. E. Lathrop, J. B. Slanina, P. Nieva, P. Zavracky, I. N. Miaoulis, and P. Y. Wong, Thermal expansion coefficient of polycrystalline silicon and silicon dioxide thin films at high temperatures, *J. Appl. Phys.* **87**, 4189 (2000).
- [42] C. Sevik, Assessment on lattice thermal properties of two-dimensional honeycomb structures: Graphene, *h*-BN, *h*-MoS₂, and *h*-MoSe₂, *Phys. Rev. B* **89**, 035422 (2014).